Development of a Stingray-inspired High-Frequency Propulsion Platform with Variable Wavelength*

Qiang Zhong¹, Yicong Fu^{1§}, Leo Liu^{1§}, and Daniel B. Quinn^{1,2}

Abstract-Undulatory fin motions in fish-like robots are typically created using intricate arrays of servo motors. Motor arrays offer impressive versatility in terms of kinematics, but their complexity leads to constraints on size, hydrodynamic force production, and power consumption, particularly when studying propulsive performance at high-frequencies. Here we present an alternative design that uses a single motor and a tunable rotary cam-train system to achieve a spectrum of fin motions running from oscillation (wavenumber < 1) to undulation (wavenumber > 1). Our platform enables thrust, lift, power, and wake measurements at prescribed pitch amplitudes, frequencies, and wavenumbers. We demonstrated the platform's oscillating and undulating capabilities via force and wake measurements in a water tank. Studies of fin wavenumber offer design insights for fish-like underwater robots, particularly those with stingray-inspired designs.

I. INTRODUCTION

When describing the extraordinary performance of swimming animals, two features that are often desirable are high speed and high maneuverability. An aquatic animal is often thought of as possessing one or the other, not both. Tuna are high-efficiency apex predators that can reach speeds of 80 kph by oscillating their caudal fins [1], but they are not very maneuverable [2]. In contrast, knifefish with undulating anal fins are comparatively slow but are some of the "most maneuverable" of all teleost fishes [3]. Oscillating fins are defined as having less than one wavelength present on the fin (wavenumber less than one), while undulating fins have more than one wavelength (wavenumber greater than one) (Fig.1b,c). For decades, scientists and engineers have developed robots and test platforms to explore the physics of oscillating and undulating fins, trying to understand how fishes have evolved swimming modes that range from high speed to high maneuverability.

Oscillating fins appear in a variety of free-swimming robots, where they are actuated by high-torque servo motors [4], [5], magnetic actuators [6], hydraulic/pneumatic actuators [7], smart materials [8], or biohybrid actuators [9]. These autonomous robots offer platforms for studying actuation systems, sensing, controller design, etc. When studying the fundamental physics of oscillating fins, researchers often approximate a fish's oscillating tail as a pitching and/or

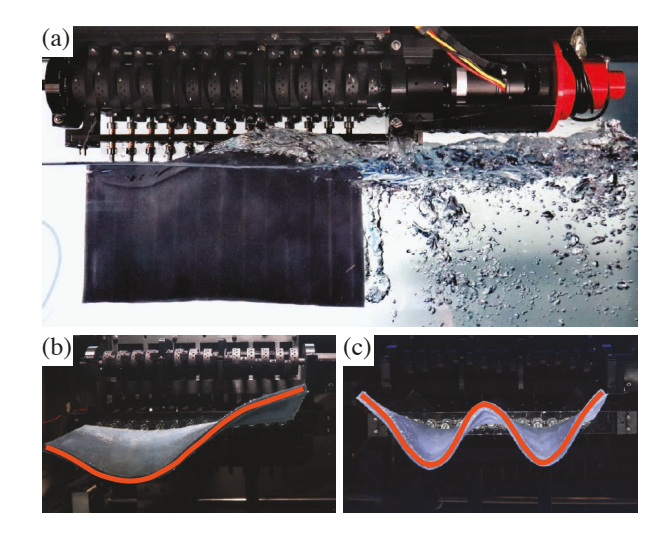


Fig. 1. **Overview of the assembled stingray-inspired platform**. (a) The platform accelerates rapidly (undulation frequency = 6 Hz) in shallow water, resulting in a strong multi-phase turbulent propulsion jet. (b) Small modular cam offsets produce low-wavenumber (oscillatory) motions. (c) High modular cam offsets produce high-wavenumber (undulatory) motions.

heaving hydrofoil [10]–[12]. The hydrofoils are typically driven by high-torque digital servo motors or stepper motors, and they are equipped with precise force sensors, leading to lower frequencies but highly repeatable motions and precise performance measurements.

Undulating fins have received less attention, presumably because they are thought to be less efficient and are harder to recreate robotically. Robots that employ undulatory motion have traditionally used arrays of motors. Thandiackal et al. [13], for example, developed an undulating swimming robot with an array of digital servo motors, capable of swimming autonomously using onboard sensor-based control. Velox [14], a ray-inspired robot developed by Pliant Energy Systems, uses two servo motor arrays to not only undulate in water but also skate on ice. Robots driven by motor arrays can easily control their frequency, amplitude, and wavenumber by altering the kinematics and phase offsets of the motors [15]. However, arrays of motors come with space and power constraints. The constraints are most severe if fluid power consumption is to be measured because multiple load cells and torque sensors must be installed on the drive shaft. As a result, undulating robotic fins have been limited to frequencies less than 3 Hz when operating at even moderate undulation amplitudes [16], [17], and their hydrodynamic power consumption is challenging to measure. One way around these constraints is to actuate fins at their leading

^{*}Research supported by the National Science Foundation (1921809 and 2040351; Program Manager: Ron Joslin)

[§]Equal contribution.

¹Department of Mechanical and Aerospace Engineering, University of Virginia, 122 Engineer's Way, Charlottesville, VA 22903, USA. Email: qiangzhong@virginia.edu, danquinn@virginia.edu

²Department of Electrical and Computer Engineering, University of Virginia, 122 Engineer's Way, Charlottesville, VA 22903, USA.

edge and rely on passive flexibility to create undulation [18], [19]. This approach offers helpful physical insights, but it cannot be used to directly study wavenumber effects.

The constraints of robotic test platforms have thus far prevented any comprehensive investigation of the physics governing the oscillation-undulation spectrum. We present here a new stingray-inspired propulsion platform that enables high-frequency, variable-amplitude, variable-wavenumber locomotion (Fig. 1). Unlike other autonomous robot designs, our platform focuses on highly controllable and precise experiments, which allows the first systematic investigation of the relationships between swimming performance (thrust, mechanical power consumption, wakes) and position along the oscillation-undulation spectrum. The rest of this paper is organized as follows: Section II, mathematical modeling of the rotary-based oscillating/undulating fin; Section III, design and construction of the platform; Section IV, acceleration force and flow measurement; Section V, preliminary performance and propulsion wake data from the platform; Section V, conclusion.

II. MATHEMATICAL MODELING

To consider the fin motions that result from our actuator, we modeled the fin as an elastic membrane attached to n pitching spines. Each spine is driven by a modular cam as follows. First, the rotary motion of the i'th cam is converted to the linear motion of the i'th sliding rod via a "Scotch-yoke joint" (joint A, Fig. 2a). The change in horizontal position of joint B on the i'th sliding rod is

$$h_i(t) = d\cos(\omega t + \phi_i),\tag{1}$$

where d is the constant distance between the center axis of the cam and the eccentric pivot, ω is the angular velocity of the cam, t is time, and ϕ_i is the initial angle of the i'th cam. A tilting and sliding joint (joint B, Fig. 2a) then convert the sliding rod's translation motion to the spine's pitching motion about joint C. The i'th spine's pitch angle is thus

$$\theta_i(t) = \arctan\left(\frac{h_i(t)}{\ell}\right) = \arctan\left(\frac{d\cos(\omega t + \phi_i)}{\ell}\right), (2)$$

where ℓ is the vertical distance between joint C and the joint B. The maximum pitch angle of the spine is

$$\theta_0 = \max[\theta_i(t)] = \arctan\left(\frac{d}{\ell}\right).$$
 (3)

Because d is constant in our model, θ_0 is fully determined by the distance ℓ . To model a complete fin, we modeled n identical rotary-based pitching actuators stacked into an array (Fig. 2b). The length of the entire fin along the x axis is L, leading to a distance of L/(n-1) between each spine. The cams are identical and connected in series, so they share the same values of d and ω . For our first set of tests, we approximated sinusoidal fin motions by using a constant phase angle offset between adjacent cams, i.e. $\phi_i = i\Delta\phi$ and

$$\theta_i(t) = \arctan(\frac{d\cos(\omega t + i\,\Delta\phi)}{\ell}),$$
 (4)

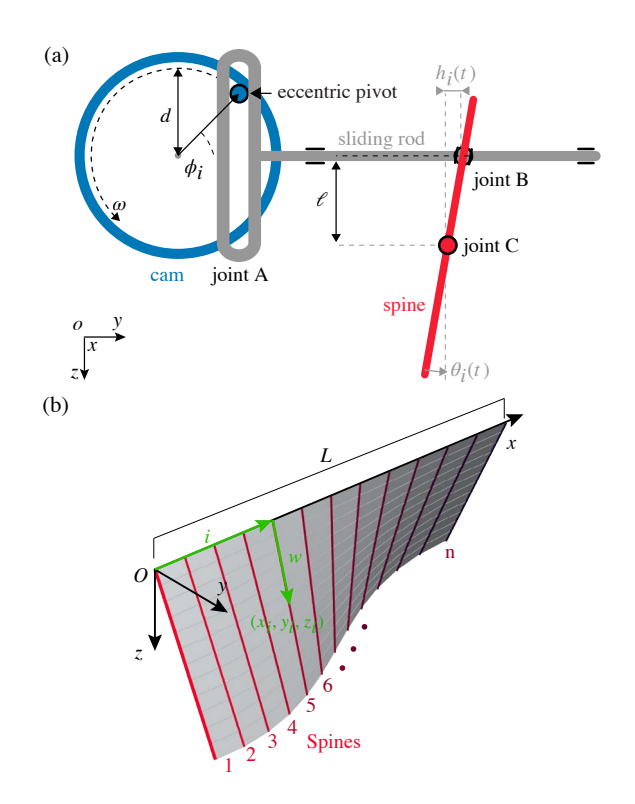


Fig. 2. Mathematical modeling of the fin kinematics. (a) Schematic of the Scotch-yoke mechanism that converts rotary cam motion into pitching spine motion. (b) A sample fin surface reconstruction based on Eq. 5 with n=13.

where $\theta_i(t)$ is the pitch angle of the *i*'th spine and $\Delta \phi$ is the phase offset between two adjacent cams. The x-, y-, and z-positions of a point on the fin's surface are

$$x_{i} = \frac{iL}{n-1},$$

$$y_{i} = w \sin(\arctan(\frac{d\cos(\omega t + i\Delta\phi)}{\ell})),$$

$$z_{i} = w \cos(\arctan(\frac{d\cos(\omega t + i\Delta\phi)}{\ell})),$$
(5)

where w is distance along the spine. The wavelength of the resulting motion is $\lambda = 2\pi L/((n-1)\Delta\phi)$, and a sample surface is shown in Fig. 2b. Note that Eq.5 converges to a continuous undulating surface as the number of spines goes to infinity. For a finite number of spines, the undulating motion is not strictly sinusoidal, but it is a close approximation when n is sufficient (n=13 in the current study). As described in Eq.5, we can independently adjust $\Delta\phi$, ℓ , and ω for wavenumber v, amplitude θ_0 , and frequency f control.

III. DESIGN OF THE STINGRAY PLATFORM

To overcome the frequency limits of servo motors, we used a rotary-based actuation strategy inspired by previous high-frequency oscillating fin studies [20], [21]. This design allows us to reach frequencies up to 7 Hz and calculate the mechanical power at a single point in the driveshaft (Fig. 3). At a glance, the stingray platform consists of 13 identical in-line modular pitching actuators which are driven by a high-torque digitally controlled DC motor. Together, these components control the frequency f, amplitude θ_0 ,

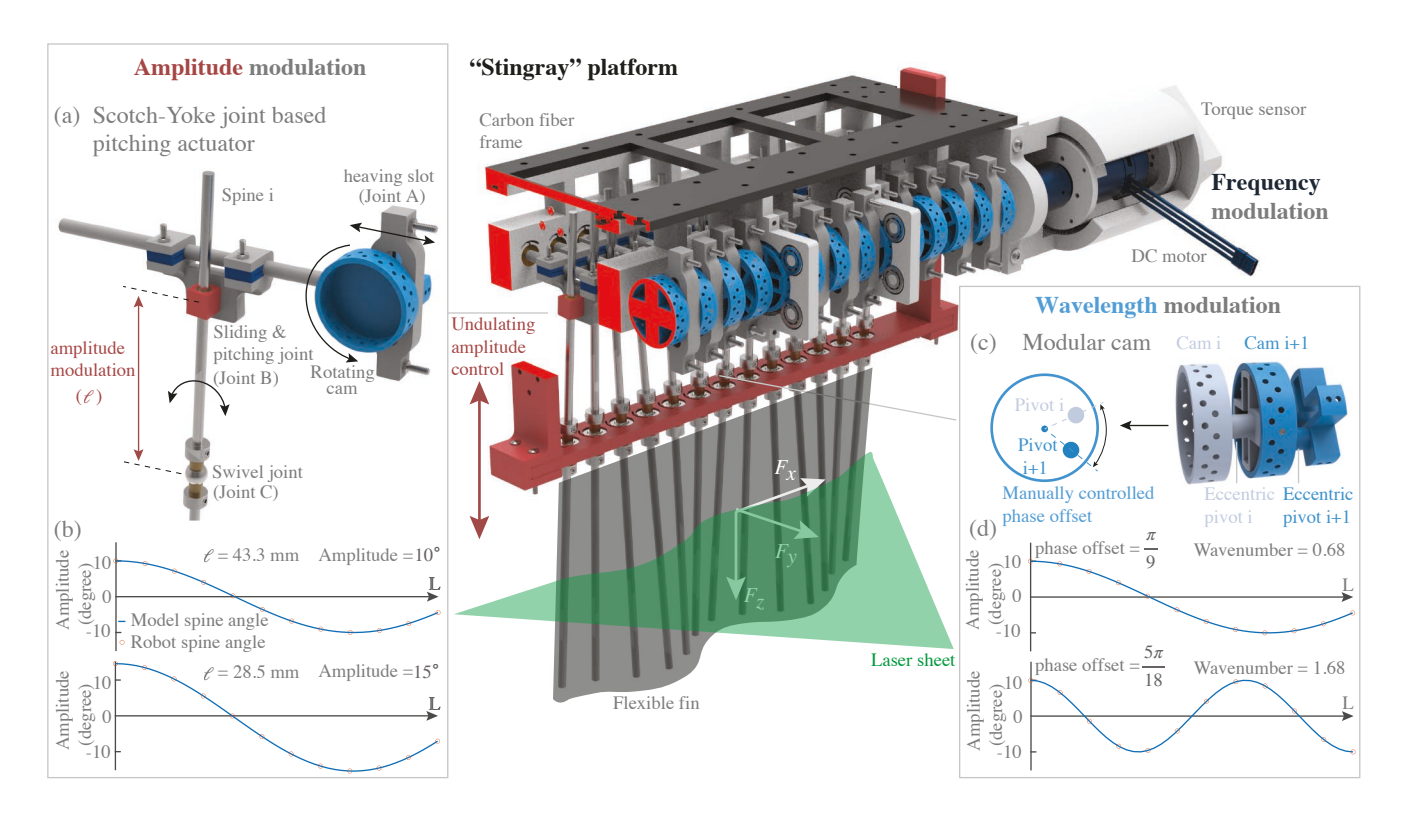


Fig. 3. **Stingray-inspired platform: actuation mechanism.** (a) Design details of the Scotch-yoke pitching actuator. (b) Fin amplitude is adjusted by controlling the relative distance ℓ between the swivel joint and the sliding & pitching joint. (c) Design details of the modular cam, showing the adjustable phase offset of the eccentric pivot. (d) Motion wavelength is manually adjusted by controlling the phase offset of the modular cams.

and wavenumber v of the fin (0.5-7 Hz, 0-20°, and 0-2, respectively).

A. SCOTCH YOKE PITCHING SPINE DESIGN

Each of the 13 pitching actuators is a modified "Scotchyoke mechanism" and has three components: a modular rotary cam, a sliding rod, and a pitching spine (Fig. 3a). Each cam has a large-radius hollow disk on one side and a small-radius cross-shaped connector on the other side, which allows a series of cams to stack together (Fig. 3c). In each cam, the hollow disk and the cross-shaped connector are connected by a rod that functions as an eccentric pivot (7.62 mm from cam center). When the cam rotates, the rotary motion is converted into a periodic heaving motion in the sliding rod with a 15.24 mm peak-to-peak amplitude (joint A, Fig. 2a, Fig. 3a). All cams and sliding rods were 3D-printed in Nylon 12 material because of its high impact resistance and low friction properties. The cam train is powered by a high-torque BLDC motor (DJI, M3508), and the rotation speed is controlled via a PWM signal from a custom onboard controller (openCM 9.04).

To convert the heaving motions of the sliding rods into the pitching motions of the spines, we designed a sliding and pitching joint that connects each sliding rod to a spine (joint B, Fig.2a, Fig.3a). The custom joint uses a plain linear bushing installed in a 3D-printed nylon hose (colored in red), which allows the spine to translate linearly along with the hose. This linear bushing hose is then connected to the "joint

frame" (colored in grey) through a rotational flange bearing, thereby allowing it to rotate as the joint frame moves with the sliding rod. Together with the swivel joint (joint C), which is fixed in position but freely to pitch 20° along the spine, this custom joint converts the heaving motion of the sliding rod into the pitching motion of the fin spine.

B. WAVELENGTH CONTROL

The fin's wavenumber is controlled by tuning the phase offset between cams. By aligning certain set screw holes between subsequent cams, we can adjust the phase offset between the cams with a resolution of $\pi/18~(10^\circ)$. The wavenumber v is then equal to $L/\lambda=6~\Delta\phi/\pi$. For example, with a phase offset of $\pi/9$, the wavenumber is 0.68, and with no phase offset, the wavenumber is zero (pure flapping motion). Although the modular cams could theoretically generate very high wavenumbers, the maximum wavenumber is limited by the stretching limit of the fin material, the internal stress the motor can drive, and the fidelity of the undulation motion profile. In our case, we confine the set of wavenumbers to $v\in [0,\frac{1}{3},\frac{2}{3},1,\frac{4}{3},\frac{5}{3},2]$, which correspond to wavelength $\lambda\in [\infty,3L,\frac{3L}{2},L,\frac{3L}{3},\frac{L}{5},\frac{L}{2}]$.

C. AMPLITUDE CONTROL

The fin's amplitude is controlled by adjusting the relative vertical distance between the swivel joint and the sliding rod (ℓ) . All thirteen swivel joints are aligned and press-fitted to the same horizontal level on a CNC-cut aluminum plate,

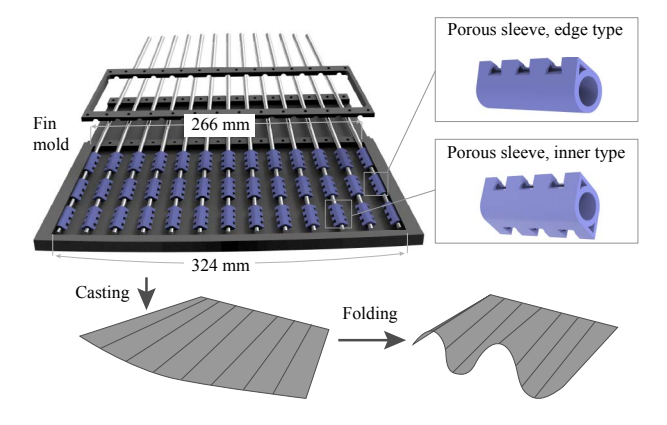


Fig. 4. Overview of the flexible fin membrane molding process

which guarantees the motion consistency among individual pitching modules and the durability of the frame during the experiment. The plate is then connected to two height-controlling hangers attached to the main platform frame (Fig. 3). Each fin spine is free to pitch around the swivel joint in all directions, and its axial position relative to the swivel joint is fixed by two shaft collars placed above and below each swivel joint. By adjusting the height of both hangers at the same time, the stingray platform is able to change the fin's amplitude (θ_0) from 0° to 20° in increments of 5° .

D. FLEXIBLE FIN MEMBRANE

Our flexible fin membrane is made of a silicone rubber (90% Ecoflex 0020 and 10% Ecoflex 0030 by weight). Real ray fins are made up of muscle fibers, neurovasculature, and collagen fibers, but the fin membrane with spines often replicate the basic physics of fish-like propulsion [22]. To mold the fin membrane, we first attached porous sleeves to 13 equally spaced stainless steel spines to promote better fin attachment to the spine, then installed the spines into a 3D-printed mold. The Ecoflex material (plus a small addition of black dye to facilitate flow visualization) was then poured into the mold. The thickness of the fin membrane is 9.5 mm, just thick enough to cover the spines with sleeve attachments.

To minimize internal stresses, we designed a skirt-shaped mold (Fig.4), such that the fin experiences no compression stresses and minimal tensile stresses as it bends into a 3D sinusoidal shape (Eq. 5). To generate the specific skirt shape of the mold, we calculated the time-varying arc length between subsequent spines given a certain amplitude and wavenumber. In general, the inter-spine arc length is minimized at the maxima/minima of the sine wave and maximized at the zeroes of the sine wave. To avoid compression stresses, we set the inter-spine separation in the mold to the minimum arc length of the sin wave predicted at that z position. Our initial skirt-shaped mold was optimized for the maximum wavenumber and an intermediate amplitude $(v=2.0; \theta_0=15^\circ)$ based on the range of the platform. The fin has a flat top of 266 mm and curved bottom of 324 mm. When installed to the stingray platform, its projected area is a rectangle with a length of 250 mm and a height of 120 mm,

giving it an aspect ratio that is typical of benthic rays [23] and enough area to generate measurable forces. We chose to start with a rectangular fin, but the molding process could easily be generalized to other platforms (i.e. triagular, elliptical).

IV. EXPERIMENTS

A. ACCELERATION FORCE AND POWER MEASURE-MENTS

To test the acceleration performance of the stingray platform, we suspended the platform in a water tank (still water) with a test section of 300mm-by-420mm-by-600mm ($W \times H \times L$). The stingray platform was tested over a range of frequencies at two selected wavenumbers.

We evaluated the acceleration performance based on direct force measurements. Due to the weight of the entire platform, we first connected the platform to a test frame with four identical sets of hinges, then installed a custom two-axis analog force sensor (T501 from Right.lnc) to measure instantaneous thrust (F_x) and lift (F_y) forces. The sensor measurement range was $5\,\mathrm{N}$ in the x direction and $10\,\mathrm{N}$ in the y direction. A data acquisition board (National Instruments, model USB-6221) with a 16-bit analog-to-digital converter sampled the sensor's signals at $100\,\mathrm{Hz}$. The sensing resolution was therefore $0.07\,\mathrm{mN}$ in the x direction and $0.15\,\mathrm{mN}$ in the y direction. We then time-averaged F_x and F_y (over $25\,\mathrm{cycles}$) to produce "net thrust", \overline{T} , and "net lift", \overline{L} .

The mechanical power consumption was calculated based on the motor rotating speed (ω) and direct torque measurements. The time-averaged power $\overline{P} \equiv \overline{\omega \tau_m}$, where τ_m is the instantaneous torque measured by a torque sensor (ATI MINI 45 IP65, SI-290-10, resolutions:1.3 mNm) installed on the base of the motor. The power consumption we measured consists of two components: external (fluid) and internal (stress and friction) consumption. We included the internal power consumption in our results since it was negligible at small amplitudes. For larger amplitude cases, we could eliminate the internal power consumption by subtracting the \overline{P} measured in the air.

Each independent trial consisted of a standby period (7s), a warm-up period (5s), an effective data collection period (25 undulation cycles), and a cool-down period (5s). We set amplitude as a constant ($\theta_0=15^\circ$) for all experiments. The experiments included two different wavenumbers (oscillation: v=0.68 and undulation: v=2.0), which are inspired by kinematics of swimming rays (*Gymnura micrura*: $v=0.64\pm0.04$ and *Dasyatis sabina* $v=1.31\pm0.12$ [23]). The swimming frequencies ranged from 0.5 Hz to 7 Hz with an increment of 0.25 Hz. Every combination of frequency and wavenumber was tested five times, resulting in a total of 270 independent trials. Cases were omitted if the measured forces and torque were out of the sensor's measurement range (30 trials with v=0.68 and f>5.5 Hz were omitted).

B. FLOW VISUALIZATION

To explore the propulsion wake of the stingray platform, we used Planar Particle Image Velocimetry (2D-PIV) to capture the in-plane velocity field at the midspan of the fin

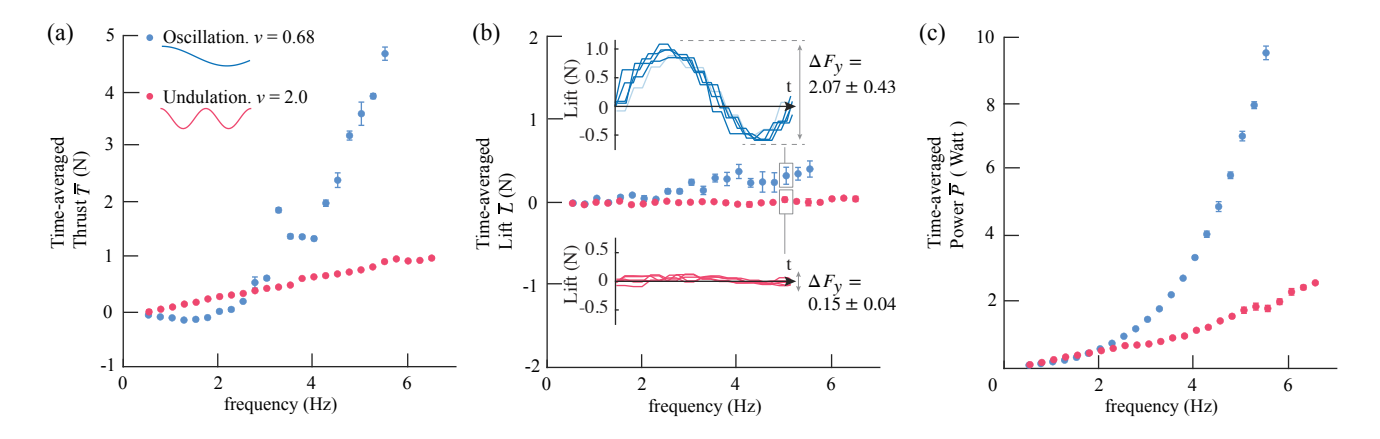


Fig. 5. Wavelength affects acceleration performance. (a) Oscillation (v=0.68) generated less thrust than undulation (v=2.0) at low frequencies (≈ 3 Hz), but more thrust at high frequencies (≈ 3 Hz). The sharp local peak around f=3.5 Hz is presumably due to a resonant surface wave in the water tank, because the peak is highly repeatable despite the kinematics of the fin being fully prescribed. Oscillation trials beyond f=5.5 Hz were omitted because the thrust overloaded the force sensor. (b) Undulation was predicted to be more stable based on time-averaged lift forces. Inserts: instantaneous lift forces for five independent trials for v=0.68 and 2.0 cases at f=5.0 Hz. (c) Oscillation required more input power to move the surrounding fluid.

(Fig.3) in a closed-loop water tunnel with a test section of 380mm-by-450mm-by-1520mm ($W \times H \times L$). The flow was set at 150 mm/s and seeded with neutrally buoyant polyamide particles ($12~\mu m$ average diameter). We fired two overlapping laser sheets (5 W Raypower MGL-W-532, and 10 W CNI MGL-W-532A) from opposite sides to illuminate entire test section. Two cameras beneath the channel recorded 30 images (2956×1877 pixel) of the particle motions (Phantom, SpeedSense M341) per undulation cycle to ensure sufficient phase resolution for wake analysis. Cross-correlations were calculated by an adaptive PIV algorithm (Dantec Dynamic Studio 6.1) with 16×16 px overlapping interrogation windows to get flow velocity field. Flow field vorticity were also calculated in Dantec Dynamic Studio and ploted in Tecplot (2021R2).

V. RESULTS

A. ACCELERATION PERFORMANCE

Thrust generation was significantly affected by the wavenumber of the fin. For the low wavenumber case we tested (v=0.68), the time-averaged thrust dipped to negative at low frequencies, then scaled roughly with frequency squared (Fig. 5a), an expected trend based on previous rigid oscillating propulsor studies [10], [11]. In contrast, the high wavenumber case (v=2.0) had a time-averaged thrust that scaled roughly linearly with frequency. As a result of these different scalings, oscillation generated less thrust at low frequencies ($<\approx 3\,\mathrm{Hz}$) but substantially more thrust at high frequencies. For example, when operating at $5\,\mathrm{Hz}$, oscillating generated a time-averaged thrust of $3.58\pm0.21\,\mathrm{N}$, almost five times as much thrust as undulating at the same frequency $(0.71\pm0.02\,\mathrm{N})$.

Oscillation and undulation also led to differing lateral/lift forces. Over the full frequency range we tested, undulation led to negligible time-averaged lift (Fig. 5b). Oscillation led to appreciable lift as the frequency increased. Instantaneous lift traces reveal a potential source of this difference (Fig.

5b), inserts): oscillation led to more than 14 times the instantaneous lift forces during undulation, which amplify any slight asymmetries in the kinematics and geometry of the fin. It remains to be seen whether the time-averaged lift is due to amplified asymmetries or a more fundamental hydrodynamic instability. Regardless of the source of the lift, the results offer insights to why undulatory motions tend to be so laterally stable [3].

In addition to producing more thrust and lift, oscillation also requires more power than undulation at the same frequencies. At low frequencies ($<\approx 3\,\mathrm{Hz}$), both motion types required about the same amount of power (Fig. 5c). As frequency increased, the power required for undulation increased linearly, stopping at just over $2\,\mathrm{W}$. The power required for oscillation increased rapidly in comparison—it was more than 5 times higher than the power required for undulation at $f=6\,\mathrm{Hz}$. The higher thrust of oscillation appears to come at the expense of lateral instabilty and low power consumption.

B. UNSTEADY PROPULSION WAKE

To explore how wavelength affects the unsteady propulsion wake, we conducted 2D-PIV on both oscillating and undulating fin at f = 3 Hz. When oscillating, the fin shed vortices with alternating sign (a reverse von Kaŕmań vortex street [24]), as expected. Each oscillation cycle produced two counter rotating vortices, creating a wide, high-speed jet pointing in the lateral direction (Fig. 6a). Behind the undulating fin, the reverse vortex street broke down into vortices with smaller sizes and intensities (Fig. 6b). As a result, the strength and size of the lateral jet flow were significantly smaller compared to those of an oscillating fin. Although both the oscillating and undulating fins produced similar levels of thrust at f = 3 Hz (Fig. 5a), the oscillating fin accelerated more of the surrounding fluid in the lateral direction, which helps to explain why the oscillating fin appeared to be less stable and require more power (Fig. 5b

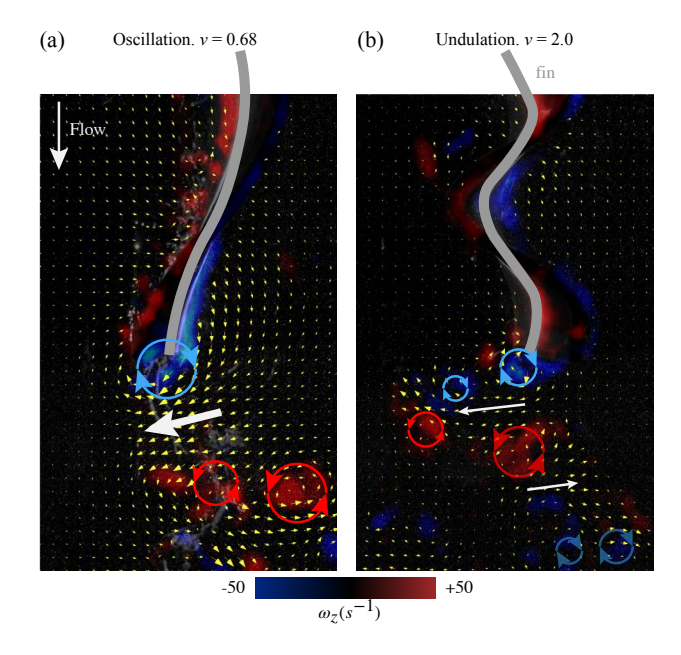


Fig. 6. Flow visualization of undulating and oscillating fins. Flow velocity field (arrows) and z-vorticity (ω_z , background color) field around the fin (grey line) of (a) oscillating case (v=0.68) and (b) undulating case (v=2.0). For both cases, the incoming flow speed was subtracted from the velocity field to highlight the unsteady propulsion wake.

and c).

VI. CONCLUSION

We have shown how a newly designed stingray-inspired platform can be used to study the continuum of fin motions between oscillation and undulation. The single-motor, adjustable-cam design offers a new way to modulate amplitude, frequency, and wavenumber, while measuring thrust, lift, power, and wake dynamics with high precision. Because the platform can adapt to different wavenumbers on an otherwise identical fin, it offers a unique way to study how wavenumber influences the speed and maneuverability of fish-like robots.

The thrust and power data taken at two different wavenumbers highlighted the functionality of the stingray-inspired platform. In these data, two wavenumbers were considered at the same amplitude and over the same frequencies. Despite using the same basic actuators, the thrust, life, and power scalings were remarkablely different for the two wavenumbers. Wake visualizations revealed the complex flow dynamics that govern these differences. Our results demonstrate how modular platforms such as ours can be used to study efficiency and stability along the oscillation-undulation/speed-efficiency spectrum.

REFERENCES

- H. B. Osmany, K. Zohra, and H. Manzoor, "New record of dogtooth tuna gymnosarda unicolor, ruppell (family: Scombridae), from pakistani water."
- [2] R. Blake, L. Chatters, and P. Domenici, "Turning radius of yellowfin tuna (thunnus albacares) in unsteady swimming manoeuvres," *Journal* of fish biology, vol. 46, no. 3, pp. 536–538, 1995.

- [3] E. D. Youngerman, B. E. Flammang, and G. V. Lauder, "Locomotion of free-swimming ghost knifefish: anal fin kinematics during four behaviors," *Zoology*, vol. 117, no. 5, pp. 337–348, 2014.
- [4] J. Yu, M. Tan, S. Wang, and E. Chen, "Development of a biomimetic robotic fish and its control algorithm," *IEEE Transactions on Systems, Man, and Cybernetics, Part B (Cybernetics)*, vol. 34, no. 4, pp. 1798–1810, 2004.
- [5] L. Wen, Z. Ren, V. Di Santo, K. Hu, T. Yuan, T. Wang, and G. V. Lauder, "Understanding fish linear acceleration using an undulatory biorobotic model with soft fluidic elastomer actuated morphing median fins," *Soft robotics*, vol. 5, no. 4, pp. 375–388, 2018.
- [6] F. Berlinger, M. Gauci, and R. Nagpal, "Implicit coordination for 3d underwater collective behaviors in a fish-inspired robot swarm," *Science Robotics*, vol. 6, no. 50, p. eabd8668, 2021.
- [7] R. K. Katzschmann, J. DelPreto, R. MacCurdy, and D. Rus, "Exploration of underwater life with an acoustically controlled soft robotic fish," *Science Robotics*, vol. 3, no. 16, p. eaar3449, 2018.
- [8] B. Kim, D.-H. Kim, J. Jung, and J.-O. Park, "A biomimetic undulatory tadpole robot using ionic polymer–metal composite actuators," *Smart materials and structures*, vol. 14, no. 6, p. 1579, 2005.
- [9] K. Y. Lee, S.-J. Park, D. G. Matthews, S. L. Kim, C. A. Marquez, J. F. Zimmerman, H. A. M. Ardoña, A. G. Kleber, G. V. Lauder, and K. K. Parker, "An autonomously swimming biohybrid fish designed with human cardiac biophysics," *Science*, vol. 375, no. 6581, pp. 639– 647, 2022.
- [10] F. Ayancik, Q. Zhong, D. B. Quinn, A. Brandes, H. Bart-Smith, and K. W. Moored, "Scaling laws for the propulsive performance of threedimensional pitching propulsors," *Journal of Fluid Mechanics*, vol. 871, pp. 1117–1138, 2019.
- [11] D. Floryan, T. V. Buren, C. W. Rowley, and A. J. Smits, "Scaling the propulsive performance of heaving and pitching foils," *Journal of Fluid Mechanics*, vol. 822, pp. 386–397, 2017.
- [12] M. S. Triantafyllou, A. H. Techet, and F. S. Hover, "Review of experimental work in biomimetic foils," *IEEE Journal of Oceanic Engineering*, vol. 29, pp. 585–594, 2004.
- [13] R. Thandiackal, K. Melo, L. Paez, J. Herault, T. Kano, K. Akiyama, F. Boyer, D. Ryczko, A. Ishiguro, and A. J. Ijspeert, "Emergence of robust self-organized undulatory swimming based on local hydrodynamic force sensing," *Science Robotics*, vol. 6, no. 57, p. eabf6354, 2021.
- [14] B. P. Filardo, D. S. Zimmerman, and M. I. Weaker, "Vehicle with traveling wave thrust module apparatuses, methods and systems," Dec. 28 2021, uS Patent 11,209,022.
- [15] O. M. Curet, N. A. Patankar, G. V. Lauder, and M. A. MacIver, "Mechanical properties of a bio-inspired robotic knifefish with an undulatory propulsor," *Bioinspiration & biomimetics*, vol. 6, no. 2, p. 026004, 2011.
- [16] L. Liu, Y. Li, Y. Wang, and X. Ma, "Design and preliminary evaluation of a biomimetic underwater robot with undulating fin propulsion," in *IOP Conference Series: Materials Science and Engineering*, vol. 790, no. 1. IOP Publishing, 2020, p. 012160.
- [17] M. Moller, A. Schappi, and P. Buholzer, "Sepios: Riding the wave of progress," in *Final Report, University of Zurich*, 2014.
- [18] D. B. Quinn, G. V. Lauder, and A. J. Smits, "Flexible propulsors in ground effect," *Bioinspiration and Biomimetics*, vol. 9, p. 8, 3 2014.
- [19] R. Fernández-Prats, V. Raspa, B. Thiria, F. Huera-Huarte, and R. Godoy-Diana, "Large-amplitude undulatory swimming near a wall," *Bioinspiration & biomimetics*, vol. 10, no. 1, p. 016003, 2015.
- [20] J. Zhu, C. White, D. K. Wainwright, V. Di Santo, G. V. Lauder, and H. Bart-Smith, "Tuna robotics: A high-frequency experimental platform exploring the performance space of swimming fishes," *Science Robotics*, vol. 4, no. 34, p. eaax4615, 2019.
- [21] Q. Zhong, J. Zhu, F. Fish, S. Kerr, A. Downs, H. Bart-Smith, and D. Quinn, "Tunable stiffness enables fast and efficient swimming in fish-like robots," *Science Robotics*, vol. 6, no. 57, p. eabe4088, 2021.
- [22] R. M. Shelton, P. J. Thornycroft, and G. V. Lauder, "Undulatory locomotion of flexible foils as biomimetic models for understanding fish propulsion," *Journal of Experimental Biology*, vol. 217, no. 12, pp. 2110–2120, 2014.
- [23] L. J. Rosenberger, "Pectoral fin locomotion in batoid fishes: undulation versus oscillation," *Journal of Experimental Biology*, vol. 204, no. 2, pp. 379–394, 2001.
- [24] T. Schnipper, A. Andersen, and T. Bohr, "Vortex wakes of a flapping foil," *Journal of Fluid Mechanics*, vol. 633, pp. 411–423, 2009.